An improved continuum-based finite-discrete element method with intra-element fracturing algorithm

Min Wang[a], Ke Gao[b], Y. T. Feng[c,*]

[a] *Fluid Dynamics and Solid Mechanics Group, Theoretical Division, Los Alamos National Laboratory, Los Alamos, NM 87545, USA*

[b] *Department of Earth and Space Sciences, Southern University of Science and Technology, Shenzhen, Guangdong 518055, China*

[c] *Zienkiewicz Centre for Computational Engineering, College of Engineering, Swansea University, Swansea, Wales SA1 8EP, UK*

Abstract

This work develops a continuum-based combined finite-discrete element method (FDEM) in the framework of the explicit finite element method in conjunction with fracture algorithms. To account for complex fracturing processes, both shear failure and tensile failure criteria are implemented. Furthermore, to investigate the effect of different fracture algorithms on the accuracy and computational efficiency of simulations, both the inter-element and intra-element fracture algorithms are developed in the continuum-based framework. Then, they are compared by two benchmark tests, of rock: the Brazilian tests and uniaxial tension tests. Besides, uniaxial compression tests under different loading rates are carried out to demonstrate the shear failure criterion and the corresponding fracture algorithm. The simulation results converge with the decrease of element sizes in the inter-element fracture algorithm. The intra-element fracture algorithm is proven to be more efficient and accurate in the simulation of fracturing processes compared to the inter-element fracture algorithm.

Keywords: finite element method, discrete element method, smeared fracture model, intra-element fracture, strain softening

1. Introduction

It has been nearly thirty years since the combined finite-discrete element method (FDEM) was first proposed by Munjiza (1992). The original aim of FDEM was to bridge the gap between the continuum simulations by the finite element method (FEM) and the discontinuous/discrete simulations by the discrete element method (DEM). Its most striking feature is to simulate the transition process from a continuous to discontinuous/discrete state in a practical manner, especially for cases under blasting and missile impact situations (Munjiza et al., 1995; Yu, 1999; Owen and Feng, 2001). To date, the FDEM has been extensively applied to various scientific and engineering problems. A recent review of its development and applications can be found in the literature (Knight et al., 2020; Rougier et al., 2020). Because of its distinct merit in modeling the fracture process of solid materials, it has been coupled with the fluid flow solver to simulate hydraulic fracture phenomenon in petroleum engineering (Fu et al., 2013; Lei et al., 2016; Wang et al., 2019; Munjiza et al., 2020), the heat transfer solver to investigate the fracture process triggered by thermal stress (Yan and Jiao, 2019; Joulin et al., 2020), and mass transfer solver to simulate the proppant migration process within fractures (Profit et al., 2016).

From the viewpoint of computational framework, the FDEM can be divided into two categories: the DEM-based FDEM and continuum-based FDEM. In the former, the update of nodal motion is element-based, and a cohesive element between meshes sharing a common edge is embedded to simulate the fracture/damage process at the very beginning of the simulation. Take a two dimensional case shown in Figure 1 for instance, the edge OP in the continuum method, e.g. FEM, will be decomposed into two edges, OP and $O'P'$, with the two pairs of end points sharing the same positions in the DEM-based FDEM. The edge OP belongs to element 2, and $O'P'$ belongs to element 1. The four-node element $OPP'O'$ is the cohesive element enclosed by dashed lines in Figure 1(b). After deformation, the nodes O and O' may depart from each other even without failure at

*Corresponding author: y.feng@swansea.ac.uk

this place. It is different from the continuum methods where there is only one point O and its displacement is exclusively determined from nodal forces. Therefore, the update of nodal motion in the DEM-based framework can be regarded as element based. Another distinct feature is the introduced cohesive element, which is the key for fracture initiation and insertion. The stress state of cohesive elements will be directly computed from the relative displacement of edges OP and $O'P'$. If the failure criteria are satisfied at the cohesive element, then a fracture can be directly inserted and represented by the cohesive element, and the linked nodes, e.g. O and O', through the cohesive elements will become independent. This fracturing algorithm is straightforward to implement for complex fracturing simulations, especially for three dimensional cases. However, fractures may only initiate and propagate along element edges/surfaces, and thus can be termed as an inter-element fracture algorithm. Normally, to secure a more accurate simulation of fracturing process, finer meshes are required, especially around fracture tips.

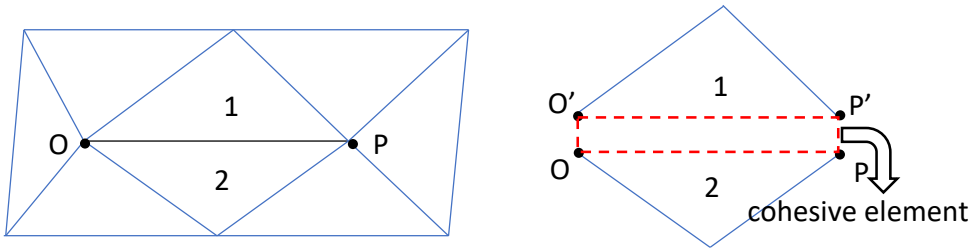

(a) line OP in the continuum mesh

(b) insertion of a cohesive element

Figure 1: Illustration of the cohesive element

The continuum-based FDEM is often based on the explicit finite element method, and no pre-embedded cohesive element is required. In this framework, the deformation of continuum is simulated by the explicit FEM. The solid is spatially discretized into meshes, and the motion of nodes, including shared nodes by neighbouring elements, is determined from Newton's second law which governs the nodal movement in the DEM-based FDEM. The calculation of element strain and stress at Gauss points also follows the finite element method. Then, based on the element stress state, fracture mechanics can be employed to handle the fracture initiation and propagation in each element. This framework has been embedded into the multifield and multiphase FEM commercial software, called ELFEN, of Rockfield Software UK. One of the earliest references of this continuum-based FDEM is Dr Yu's PhD thesis (Yu, 1999). Since then, more research work has been conducted based on this framework in (Han et al., 2000; Owen and Feng, 2001; Klerck et al., 2004; Fu et al., 2013; Profit et al., 2016), and also in (Hamdi et al., 2014; Ju et al., 2018; Wang et al., 2019). In Yu (1999), a nodal fracture algorithm was proposed to insert fractures through elements. Fractures can propagate between or through elements depending on the nodal failure direction, which is termed as the intra-element fracture algorithm. However, only tensile failure was considered in these work.

Several fracture procedures have been proposed for the FDEM and they can be roughly divided into the inter-element fracture algorithm and the intra-element fracture algorithm, according to the way that fracture is implemented. The DEM-based FDEM with cohesive elements falls into the former. In the continuum-based framework, both inter- and intra-element fracture algorithms can be realized. The fracture algorithm in FDEM is an important aspect directly associated with the efficiency of fracture simulations. The inter-element fracture is simple to implement, but requires relatively fine element meshes to ensure accuracy. Detailed discussion on the sensitivity of mesh size can be found in (Munjiza et al., 1999; Munjiza and John, 2002; Guo et al., 2016). In contrast, the intra-element fracture allows fractures to initiate and propagate orthogonal to the failure direction, and may pass through the elements. Compared to the inter-element fracture algorithm, the intra-element fracture algorithm is a more efficient way to obtain an accurate fracture simulation. However, the fracture insertion process is not straightforward, especially in three-dimensional cases. The combination of the intra-element fracture and local remeshing technique around the fracture tip is more powerful in practical engineering and scientific simulations (Han et al., 2000; Owen and Feng, 2001; Klerck et al., 2004; Fu et al., 2013; Profit et al., 2016).

It should be mentioned that the FDEM research group at Lawrence Livermore National Laboratory initially followed the DEM-based FDEM in the 1990s (Morris et al., 2006), then adopted the continuum-based framework with an improved inter-element fracture algorithm (Settgast et al., 2017). Strictly speaking, the continuum-based FDEM has a solid foundation of continuum mechanics, therefore is theoretically more rig-

orous. Its combination with the intra-element fracture algorithm and adaptive remeshing is more efficient in both computational cost and numerical accuracy. However, in addition to the difficulty in the implementation of the intra-element fracture algorithm, the adaptive remeshing technique is more challenging. Hence, most of the fracture simulations based on the continuum framework are mainly performed using the commercial software, ELFEN (Rockfield, 2004).

The primary aim of this work is to improve the existing continuum-based FDEM, where currently only tensile failure/fracture is considered, by incorporating the shear-dominated failure criterion. Furthermore, to investigate the effect of different fracture algorithms on the accuracy and efficiency of fracture simulations, both the inter-element and intra-element fracture algorithms are developed. Particularly, an adaptive intra-element fracture algorithm accounting for shear failure fractures is proposed. A detailed introduction to the primary aspects of the continuum-based FDEM used in this work is given in Section 2. Then, two numerical examples, Brazilian tests and uniaxial tension tests of rock, are carried out to explore the influence of fracture algorithms on the simulations of fracturing process. Uniaxial compression tests under different loading rates are also carried out to demonstrate the shear failure criterion and corresponding fracture algorithm in Section 3. Discussions on the new findings of this work are conducted in Section 4 before a conclusion is drawn in the last section.

2. Continuum-based FDEM

The continuum-based FDEM takes fully advantage of the explicit FEM. It discretizes the computational domain into fine meshes/elements, so-called spatial discretization. Evolution of the deformation process of the continuum under consideration is discretized into many time increments, so-called time discretization. A small time step is selected such that within each time increment, the acceleration and velocity can be regarded as constant. Since the state evolution (dynamic equilibrium equation) of the model is advanced explicitly using Newton's second law, iterations and tolerances used in implicit FEMs are not required.

In the continuum-based FDEM, the solution of dynamic equilibrium equation is node-based. In each time step, the motion of nodes can be determined by Newton's second law, which is followed by the calculation of strain of the element and subsequent stress calculation of Gauss points using constitutive models. Then, the fracture mechanics can be used to insert fractures in places where the selected failure criteria are satisfied. Based on the computed element stresses, the nodal internal force can be computed and assembled. Meanwhile, the external force applied to each node can be obtained from boundary loading conditions and/or the contact forces from other discrete/discontinuous bodies in contact. In the rest of this section, main key aspects of the continuum-based FDEM will be introduced in detail. As to the discrete contact interaction, it is the same as the one in the DEM-based FDEM (Munjiza et al., 1995; Munjiza, 2004), and its latest progress can be found in (Feng and Tan, 2020; Feng, 2021).

2.1. Motion of nodes

The deformation of the system is accomplished by updating the motion of all mesh nodes using Newton's second law

$$\boldsymbol{M}\ddot{\boldsymbol{u}}(t) + \boldsymbol{C}\dot{\boldsymbol{u}}(t) = \boldsymbol{P}^{ext} + \boldsymbol{P}^{int}, \tag{1}$$

where $\boldsymbol{M}$ is the mass matrix, $\boldsymbol{C}$ is the damping matrix, $\boldsymbol{P}^{ext}$ and $\boldsymbol{P}^{int}$ are the external force and the internal force, respectively, applied to the node. The internal force $\boldsymbol{P}^{int}$ applied to a node is calculated from the stress $\boldsymbol{\sigma}$ obtained from constitutive models and shape function $\boldsymbol{N}$ of elements sharing the node. $\ddot{\boldsymbol{u}}$ and $\dot{\boldsymbol{u}}$ are the acceleration and velocity, respectively. In the explicit algorithm, the acceleration $\ddot{\boldsymbol{u}}_i(t)$ of node i is determined by equation (1), and its velocity $\dot{\boldsymbol{u}}_i(t + \frac{\Delta t}{2})$ is updated using the central difference scheme as follows:

$$\dot{\boldsymbol{u}}(t + \frac{\Delta t}{2}) = \dot{\boldsymbol{u}}(t - \frac{\Delta t}{2}) + \ddot{\boldsymbol{u}}(t)\frac{\Delta t(t) + \Delta t(t + \Delta t)}{2}. \tag{2}$$

Then, the displacement $\boldsymbol{u}_i(t + \Delta t)$ of node i can be calculated by

$$\boldsymbol{u}(t + \Delta t) = \boldsymbol{u}(t) + \dot{\boldsymbol{u}}(t + \frac{\Delta t}{2})\Delta t(t + \Delta t). \tag{3}$$

2.2. Constitutive models

Based on the nodal displacement, the next step is to calculate the element strain and then calculate stress of each element based on the constitutive model used. In the framework of elasto-plastic constitutive models, the incremental total strain $\Delta\boldsymbol{\varepsilon}$ can be decomposed into an elastic component $\Delta\boldsymbol{\varepsilon}^e$ and a plastic component $\Delta\boldsymbol{\varepsilon}^p$ by

$$\Delta\boldsymbol{\varepsilon} = \Delta\boldsymbol{\varepsilon}^e + \Delta\boldsymbol{\varepsilon}^p. \tag{4}$$

For the strain-controlled loading conditions, the incremental stress $\Delta\boldsymbol{\sigma}$ can be computed by

$$\Delta\boldsymbol{\sigma} = \boldsymbol{D}\Delta\boldsymbol{\varepsilon}^e, \tag{5}$$

where $\boldsymbol{D}$ is the elastic modulus matrix. During each time step, the incremental plastic strain can be calculated from the flow rule, and its general form is given by

$$\Delta\boldsymbol{\varepsilon}^p = d\lambda\frac{\partial\Phi}{\partial\boldsymbol{\sigma}}, \tag{6}$$

where $d\lambda$ is the plastic multiplier, and Φ is the plastic potential function.

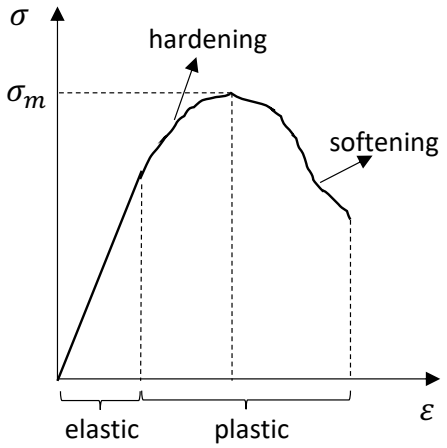

Figure 2: Elasto-plastic mechanical behavior of a material

In the whole mechanical response of materials, the plastic deformation can have two phases (see Figure 2), the hardening stage and/or the softening stage. In the hardening stage, the plastic multiplier can be obtained by

$$d\lambda = \frac{\partial f}{\partial\boldsymbol{\sigma}}\frac{\Delta\boldsymbol{\sigma}}{H_p}, \tag{7}$$

where f is the yield function. In this work, a non-associated flow rule and a deviatoric hardening law (Pietruszczak, 2010; Pande et al., 2020) are adopted. The yield function and the plastic potential function are respectively defined as

$$f = \sqrt{3}\overline{\sigma} - \eta(\varepsilon_q^p)\sigma_m g(\theta), \tag{8}$$

$$\Phi = \sqrt{3}\overline{\sigma} + \eta_c\sigma_m g(\theta)\ln(\frac{\sigma_m}{\sigma_m^0}), \tag{9}$$

where $\overline{\sigma}$, σ_m and θ are stress invariants (Pietruszczak, 2010). The hardening parameter $\eta(\varepsilon_q^p) = \eta_f\frac{\varepsilon_q^p}{A+\varepsilon_q^p}$ is a function of the deviatoric plastic strain (ε_q^p). η_f and η_c are the failure slope and the zero-dilantancy slope respectively. A is a material constant related to hardening. The convex function $g(\theta)$ associated with the angle of internal friction (ϕ) is given by

$$g(\theta) = \frac{3-\sin\phi}{2\sqrt{3}\cos\theta - 2\sin\theta\sin\phi}. \tag{10}$$

H_p in equation (7) is the plastic hardening modulus given by

$$H_p = -\frac{\partial f}{\partial \varepsilon_q^p}\frac{\partial \Phi}{\partial \overline{\sigma}}. \tag{11}$$

In the softening stage, the plastic multiplier becomes

$$d\lambda = \frac{\partial F}{\partial \boldsymbol{\sigma}}\frac{\Delta \boldsymbol{\sigma}}{H_p}. \tag{12}$$

where F is the failure function. For materials with brittle failure, a linear softening law associated with the fracture energy is commonly used (Bažant and Oh, 1983; De Borst, 1986; Klerck et al., 2004; Profit et al., 2016). Therefore, in the strain-softening stage equation (6) can be simplified as

$$\Delta \boldsymbol{\varepsilon}^p = -H\Delta \boldsymbol{\sigma}, \tag{13}$$

where H is the softening slope determined from the material strength ($\boldsymbol{\sigma}_m$), the element characteristic length (l_c) and the fracture energy release rate (G_f) by

$$H = \frac{{\sigma_m}^2 l_c}{2G_f}. \tag{14}$$

2.3. Fracture criteria and fracture algorithm

The failure behavior of solid materials is rather different. For most brittle materials, such as rock, concrete and glass, tensile failure/fracture is most common. Under confining conditions, they may exhibit shear or compressive failure/fracture from the macroscopic viewpoint. In this work, both shear and tensile fractures are considered.

In geomechanics, the Mohr-Coulomb failure criterion is the most commonly used shear failure criterion. It postulates a linear relationship between the shear stress ($\boldsymbol{\tau}$) and the normal stress ($\boldsymbol{\sigma}_n$),

$$\boldsymbol{\tau} = c - \boldsymbol{\sigma}_n \tan\phi, \tag{15}$$

where c is the cohesion. Its specific form in terms of stress invariants is given by

$$F = \frac{\overline{\sigma}}{g(\theta)} - \frac{2\sqrt{3}\sin\phi}{3-\sin\phi}\sigma_m - \frac{2\sqrt{3}c\cos\phi}{3-\sin\phi} = 0. \tag{16}$$

It is noted that the Mohr-Coulomb criterion employs two material constants c and ϕ. Both of them can be obtained from basic laboratory tests.

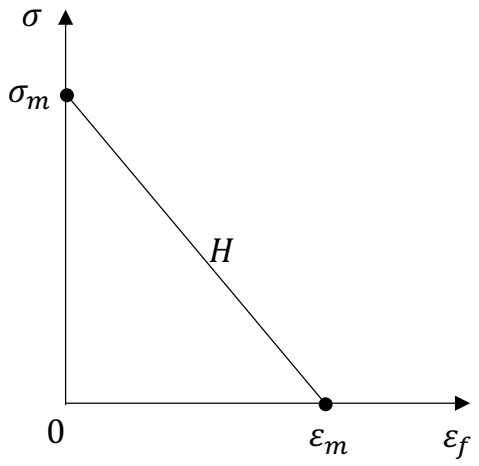

Figure 3: Linear softening law

For tensile and compressive failures, a smeared fracture model with a linear softening law is commonly used to simulate the fracture process. The idea of the smeared fracture model is to replace the physical process of

discrete cracks in a control volume, e.g. a finite element, by inserting a continuous fracture after the strain softening stage. It rationalizes the relationship between the softening slope and the fracture energy release rate using equation (14) such that the energy dissipated in the discrete and smeared failure process is equivalent. In the softening stage, the failure strain $\boldsymbol{\varepsilon}_f$ ($\boldsymbol{\varepsilon}_f = 0$, when $\sigma = \sigma_m$) will be accumulated. The failure criterion is satisfied when the maximum failure strain $\boldsymbol{\varepsilon}_m$ is reached (see Figure 3). The maximum failure strain is calculated by

$$\boldsymbol{\varepsilon}_m = \frac{\sigma_m}{H}. \tag{17}$$

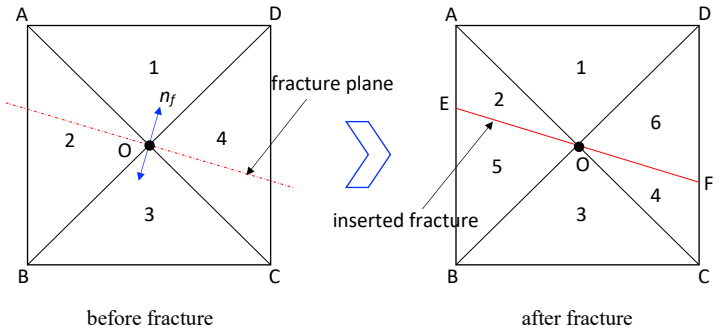

Figure 4: Intra-element fracture algorithm

When the above failure criteria are satisfied, a virtual smeared fracture will be inserted into the physical element using a specific fracture algorithm. In the DEM-based FDEM, nodal failure is first examined by the cohesive elements. Then, fracture insertion will be performed by the removal of cohesive elements at the failure places shown in Figure 1. In contrast, the process of fracturing in the continuum-based FDEM is approached by fracture mechanics. The failure criteria are examined at each node, and two fracture algorithms can be used. One is the inter-element fracture algorithm (Munjiza et al., 1995) used in the DEM-based FDEM. To better simulate the fracture propagation, an improved inter-element fracture algorithm by the inclusion of middle points of element edges was developed to improve fracture simulations (Fu et al., 2013; Settgast et al., 2017). The other is the intra-element fracture algorithm, in which the fracture propagates orthogonal to the direction of the nodal maximum tensile strain (Yu, 1999; Klerck et al., 2004). Next, we will propose an improved intra-element fracture algorithm, in which the shear failure induced fracture is also considered, and its primary steps are as follows:

1) Since the strain and stress state of each element has been determined using constitutive models, we need to first map the strain and stress of each node from Gauss points of surrounding elements;

2) According to the nodal stress state, we will first identify shear failure nodes using the Mohr-Coulomb criterion described by equation (16);

3) Then, we need to check whether tensile or compressive failure occurs at other undamaged nodes using the element size dependent maximum failure strain $\boldsymbol{\varepsilon}_m$;

4) Once all failure nodes are determined, the failure direction $\boldsymbol{n}_f$ at each failure node is defined as the direction of tensile/compressive strain. The fracture propagation direction, i.e. fracture plane, is orthogonal to the failure direction. Figure 4 shows a local case of the intra-element fracture algorithm with node O being the failure node. In most cases, the fracture plane will penetrate through the surrounding elements. Then a continuous fracture connecting two intersections, e.g. E and F, along the fracture plane can be inserted;

5) To avoid abnormal elements, such as needle-shaped element, created by the intra-element fracture algorithm, we need to separately examine the intersection angle between the fracture plane and the adjacent edge sharing the same failure node, O. Take Figure 4 for an example, if the intersection angle between edges OA and OE is less than 6°, the fracture will be forced to propagate along edge OA instead of OE.

6) The final step is to update the element mesh based on the inserted fractures, and to initialize the associated data at the failure nodes.

In some cases, the above intra-element fracture algorithm could result in the creation of very slender elements which will lead to an extremely small time step and subsequent expensive computational costs. Step 5 above provides a way to overcome such issues, which is simpler to implement for 2-d cases for most

researchers. Particularly, a more stringent but challenging method, local or global remeshing technique, can be employed to avoid very small time step (Yu, 1999; Klerck et al., 2004). In this work, we will focus on the key role of the intra-element fracture algorithm in accurate fracture simulations and computational efficiency over the inter-element fracture algorithm in the framework of continuum-based FDEM.

3. Numerical experiments

In this section, we will first investigate the effect of the fracture algorithms mentioned above on the simulation accuracy and computational efficiency in the framework of continuum-based FDEM using two benchmark tests, the Brazilian test and the uniaxial tension test of rock. Then, to further demonstrate the shear failure criterion and the corresponding fracture algorithm, uniaxial compression tests under different loading rates are carried out. The numerical examples are conducted by our in-house code developed based on the explicit element method in this work.

3.1. Brazilian tests

In the first benchmark, a circular disk of rock will undergo compression by upper and lower jaws which move toward each other (see Figure 5). The diameter (D) of the rock disk is 100 mm; the Young's modulus and Poisson's ratio of the rock under consideration are 12.0 GPa and 0.26 respectively; the bulk density is 2.6 g/cm^3; the uniaxial tensile and compressive strengths are 4 MPa and 100 MPa, respectively; the angle of internal friction is 40°, and the hardening parameter A used in the deviatoric hardening plastic model is 0.002. The fracture energy release rate (G_f) is 3 N/m. For the jaws, only elastic behavior is considered in this work. Their Young's modulus and Poisson's ratio are selected as 200 GPa and 0.29 respectively; the density is 8.0 g/cm^3. To deal with the contact interaction between rock blocks caused by fracturing, a linear normal contact model with the normal penalty (normal stiffness) equal to 1.2 $GPa \cdot m$ is applied. A Coulomb friction model is adopted to solve the tangential interaction with the tangential penalty and the friction coefficient being 0.12 $GPa \cdot m$ and 0.5. While for the contact between the jaws and the rock, the normal penalty and the tangential penalty are 20 $GPa \cdot m$ and 2.0 $GPa \cdot m$. The friction coefficient is 0.5.

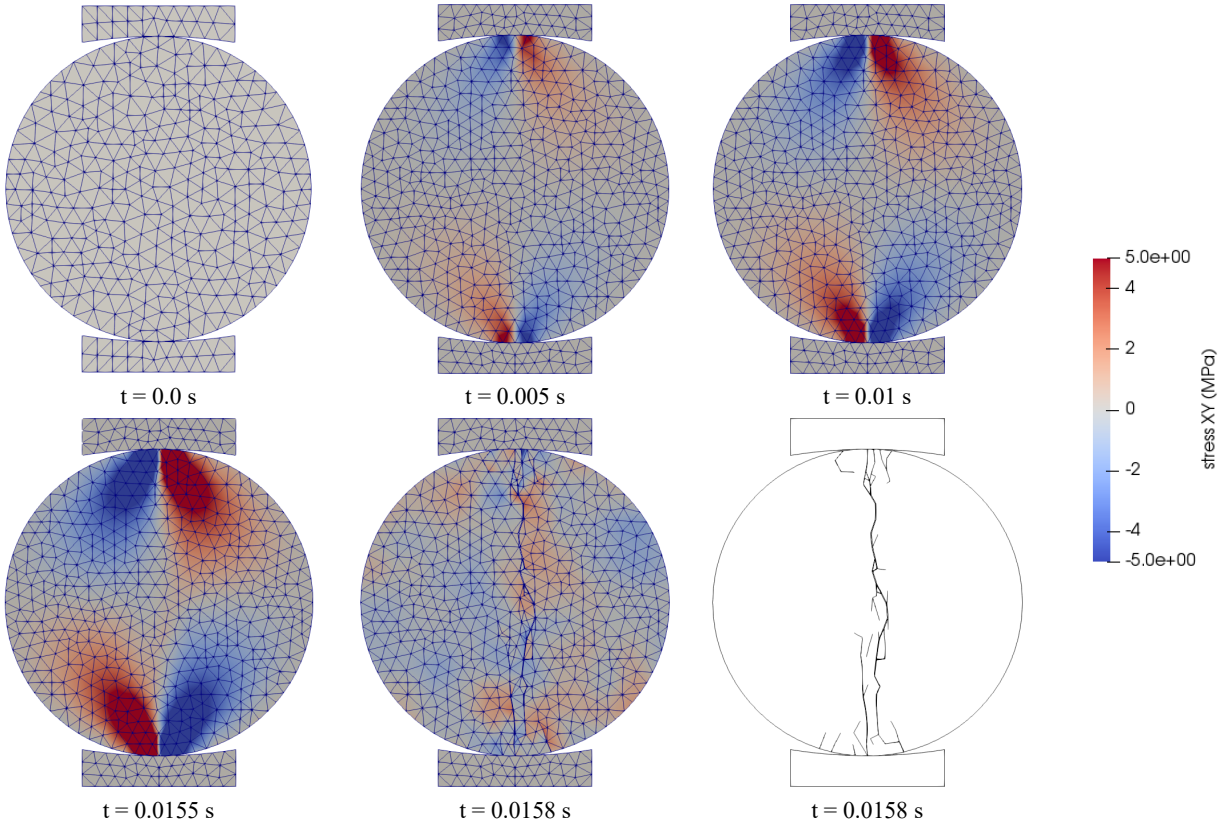

Figure 5: Snapshots of stress ($\boldsymbol{\sigma}_{xy}$) contour and fractures of Brazilian tests with intra-element fractures

The displacement-controlled loadings with a constant speed 7.5 mm/s for the upper and lower jaws are applied at the same time. To investigate the effect of the fracture algorithms on the fracturing simulation, two groups of Brazilian tests using the inter-element and intra-element fracture algorithms are carried out, respectively. In each group, various mesh sizes with characteristic length (l_c) being 5, 4, 2 and 1 mm are adopted. Snapshots of the stress contours of the rock sample with the intra-element fracture algorithm and the characteristic length of mesh being 4 mm at different time instants are shown in Figure 5. With the progress of loading, the magnitude of stress within the rock sample is increasing gradually. The initiation of fracture occurs after 0.0155 s. From the snapshot at 0.0158 s, intra-element fractures can be clearly observed.

The variation of the contact force (P) during the compression process between the upper jaw and the rock sample is given in Figure 6(a) in the simulation with the intra-element fracture algorithm and the characteristic length of mesh equal to 4 mm. The relationship between the compressive force and the tensile stress ($\boldsymbol{\sigma}_t$) is described by (Li and Wong, 2013)

$$\boldsymbol{\sigma}_t = \frac{2P}{\pi D h}. \tag{18}$$

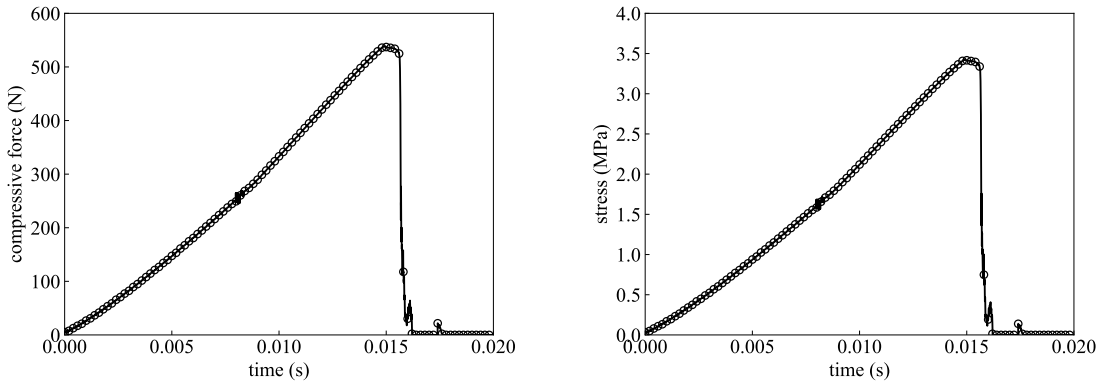

(a) force applied to upper jaw

(b) tensile stress of the sample

Figure 6: Mechanical response of the sample

In the above equation, the unit of the diameter (D) of the rock sample and its thickness (h) is mm. The units of compressive force (P) and tensile stress ($\boldsymbol{\sigma}_t$) are N and MPa, respectively. The converted stress is shown in Figure 6(b), where a brittle failure mode can be observed.

Next, we investigate the effect of mesh size on the continuum-based FDEM with the inter-element fracture algorithm. The fracture distribution within the rock sample at the end of four simulations using the inter-element fracture algorithm with different mesh sizes is given in Figure 7, where the mesh topology is clearly shown. For the models with larger mesh sizes, obvious fracture propagation along element edges can be seen. To distinguish the mesh and the fracture distribution, the obvious fracture patterns are highlighted in red in Figure 7 using the mode of feature edges. It is found that the distribution of primary fractures in the simulations with mesh sizes of 2 mm and 1 mm is similar. While in the simulations with larger mesh sizes the fracture is significantly different from those in the simulations with smaller mesh sizes. In addition to the fracture distribution, we further compare the stress-strain response of simulation with different mesh sizes in Figure 8. The corresponding numerical errors of tensile strength are calculated with the value obtained from the smallest element size being the reference strength, and are shown in Figure 9. We can also find the similar phenomenon as observed in fracture distribution that the tensile strength converges with the decrease of element size.

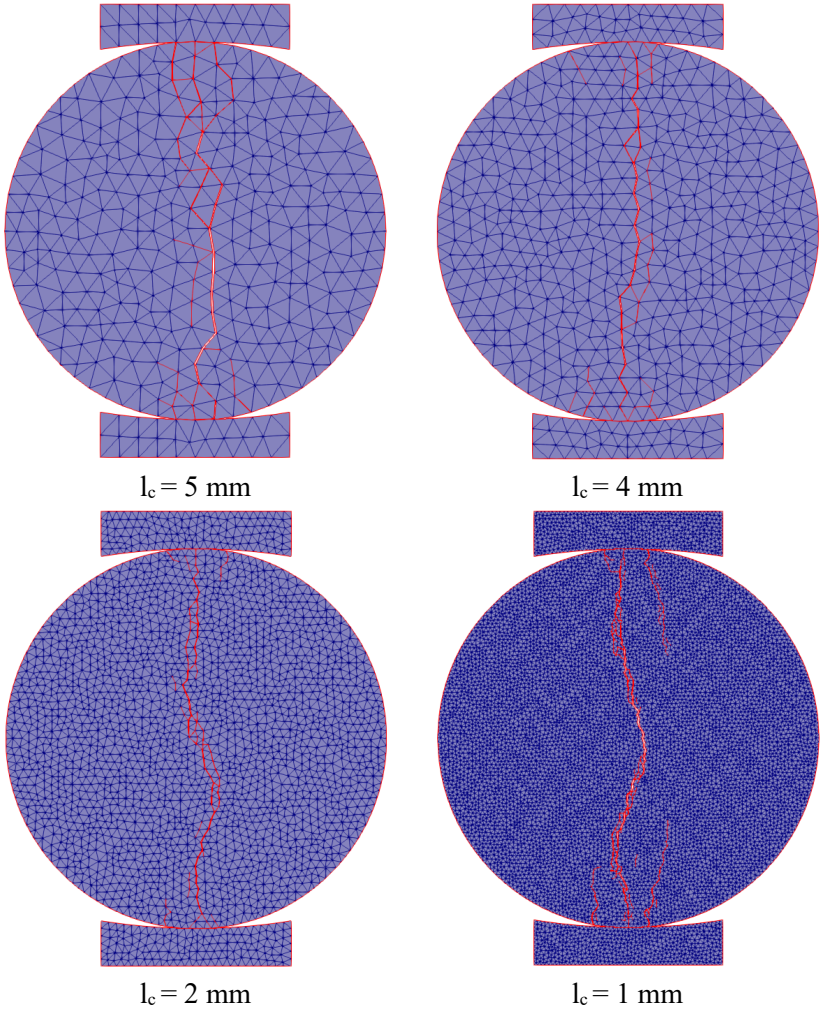

Figure 7: Fracture distribution in models using inter-element fracture

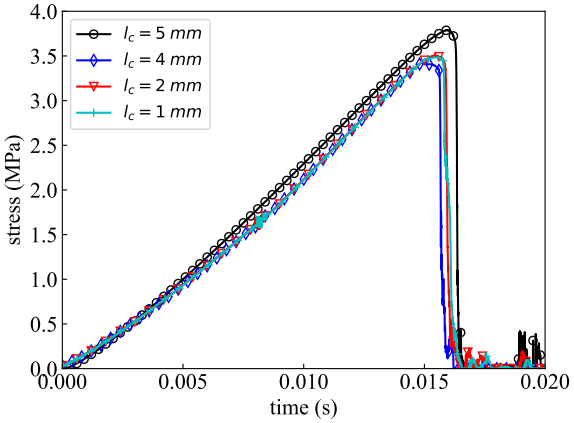

Figure 8: Comparison of stress-strain behavior under different element sizes

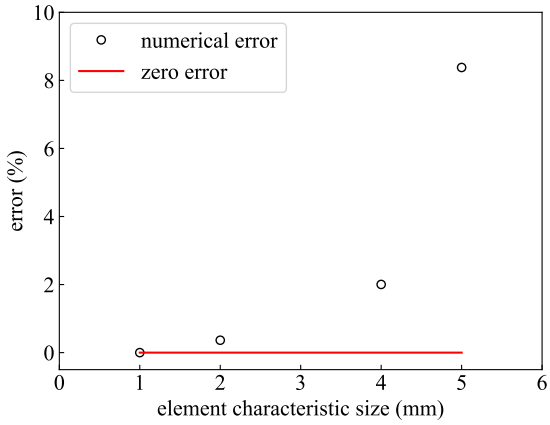

Figure 9: Effect of element size on numerical error of tensile strength

To compare the inter-element and intra-element fracture algorithms on the numerical Brazilian tests and evaluate the efficiency of the latter, we compare the fracture distribution in the simulations using the intra-element fracture algorithm with different element sizes in Figure 10, where fracture distributions are highlighted in red again. We can see in the simulations with the characteristic size of 5 mm and 4 mm, smaller elements are created due to the intra-element fracture algorithm. However, with the decrease of element size no obvious intra-element fractures can be found in the simulation with the characteristic size being 2 mm. For the simulations with the characteristic size of 2 mm but different fracture algorithms, their fracture patterns are almost the same as shown in Figure 11, where the differences are marked using white circles. For the simulations with larger element sizes, the introduction of the intra-element fracture algorithm renders the fracture distribution closer to that in the fine-element simulation. Although there are still some differences, it is much better than the one obtained by the inter-element fracture algorithm.

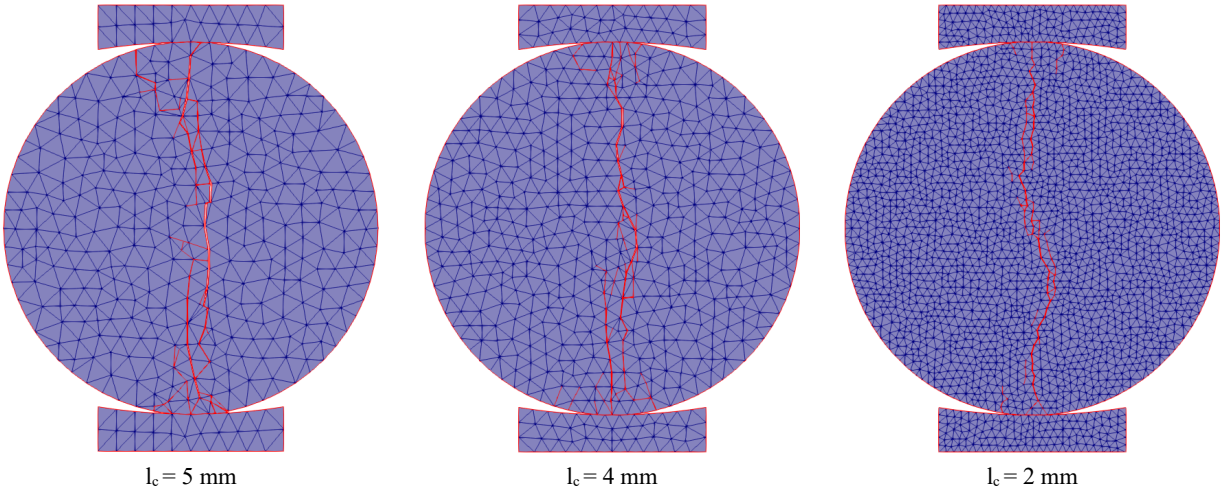

Figure 10: Comparison of failure of models using the intra-element fracture

The effect of element size on the tensile strength is shown in Figure 12, where both inter- and intra-element fracture algorithms are accounted for. Compared to the inter-element fracture algorithm, the intra-element fracture algorithm can improve the accuracy of tensile strength to a certain degree when the element size is relatively large.

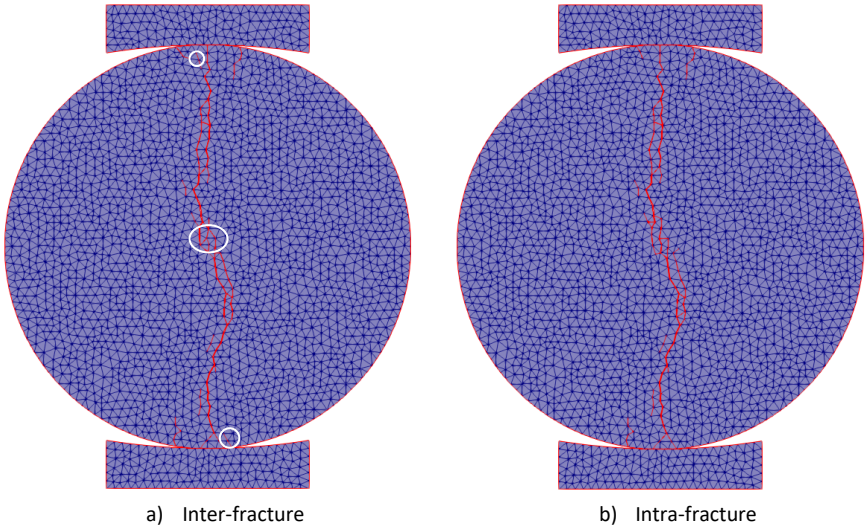

Figure 11: Comparison of fracture distribution simulated by different fracture algorithms ($l_c = 2\ mm$)

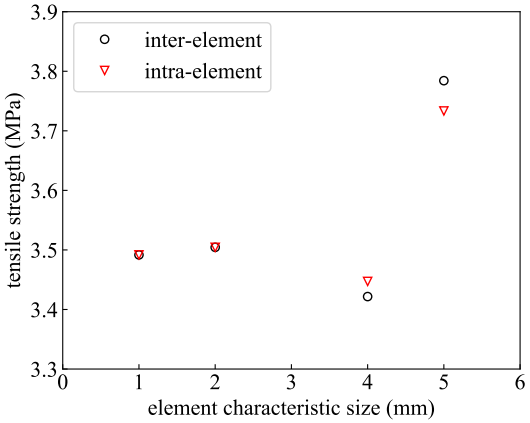

Figure 12: Effect of element size on tensile strength

3.2. Uniaxial tension tests

We further evaluate the intra-element fracture algorithm using uniaxial tension tests of rock. The size of the rock sample is 100 mm × 200 mm. All material parameters of rock and contact models are the same as those used in the above Brazilian tests. The displacement-controlled loadings with constant speed 7.5 mm/s are applied to the nodes at the top and bottom boundaries of the rock sample. As neither platens nor jaws are used in this tension test, the stress-strain curve is not available, and we will focus on the fracturing process in this benchmark.

We compare the fracture distribution in the simulations with the inter-element fracture algorithm and three element characteristic sizes in Figure 13, where the vertical displacement contour of rock samples before and after fracturing process are shown. In this benchmark the effect of element size on fracture distribution is more remarkable for the simulations using the inter-element fracture algorithm. Then, we further investigate the element size effect on the simulations using the intra-element fracture algorithm. The fracture distribution at the end of the simulations of different element sizes is shown in Figure 14. Again, it is evident that fractures propagate through elements in the simulations with characteristic length being 10 mm and 6.5 mm. It is clear that the fracture distribution in the simulations with the element characteristic length being 10 mm and 6.5 mm is similar to the one in the simulation with the fine element size when the intra-element fracture algorithm is utilized to simulate the fracturing process, which indicates that the intra-element fracture algorithm has obvious influence on the simulations of fracturing process with relatively large element sizes.

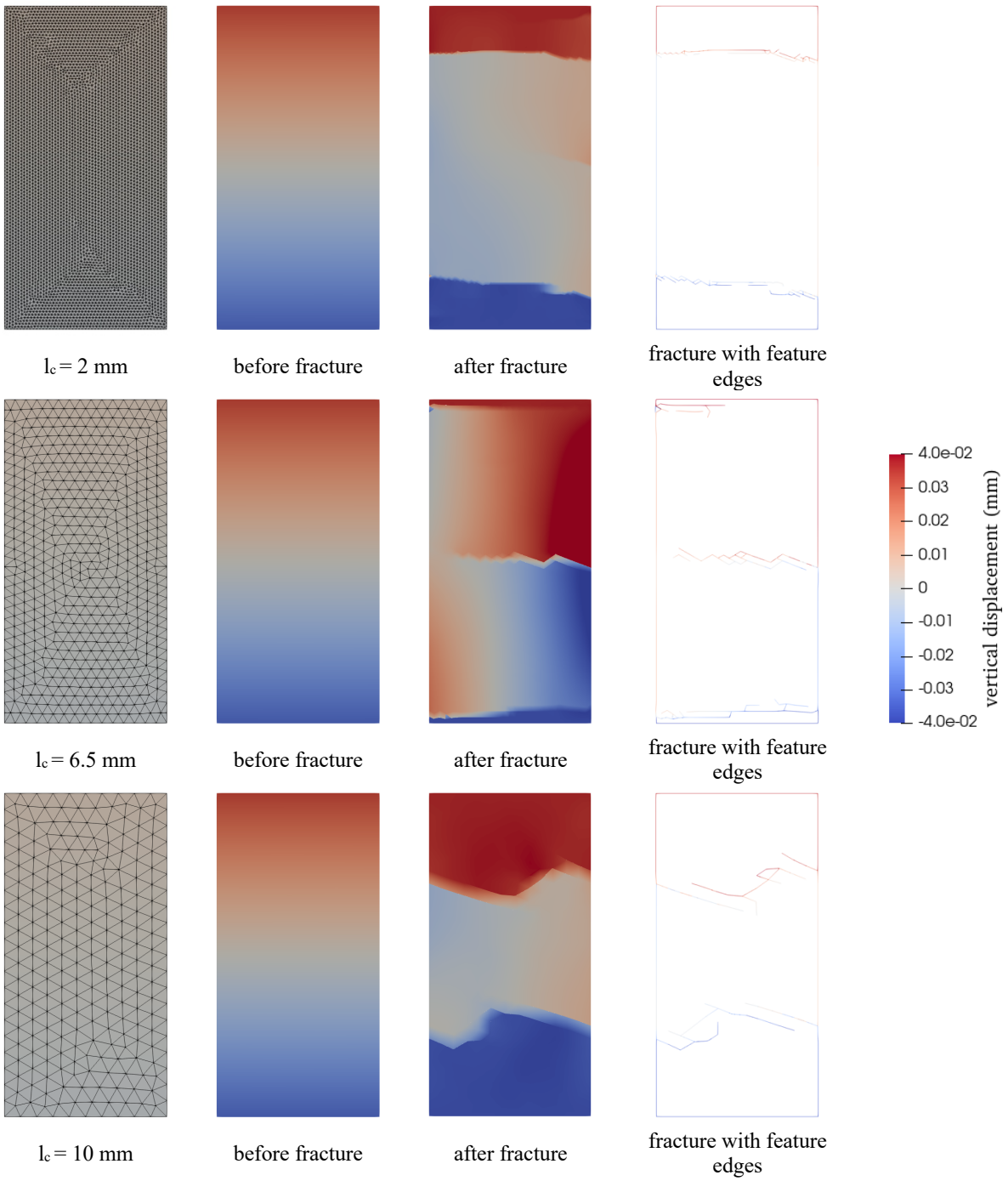

Figure 13: Size effect on failure process for the inter-element fracture models

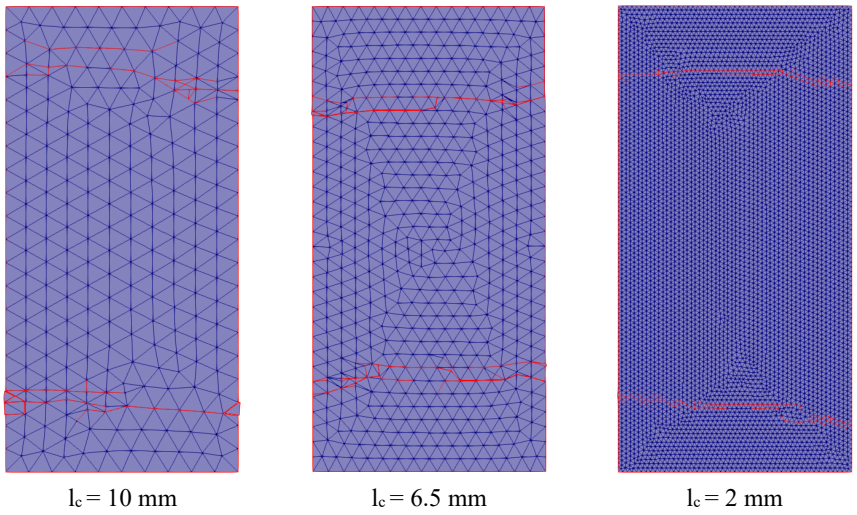

Figure 14: Fracture distribution of models with intra-element fracture

3.3. Uniaxial compression tests

The above Brazilian tests and uniaxial tension tests of rock clearly demonstrate the importance and efficiency of the intra-element fracture algorithm. Next, the proposed FDEM will be further used to investigate the initiation and propagation of shear failure induced fractures using uniaxial compression tests of rock under different loading rates.

As shown in Figure 16, the rock sample with size 100 mm × 200 mm will be compressed by two parallel platens moving towards each other. The mechanical parameters of the platens and the rock sample are almost the same as those in the Brazilian tests, except that the Young's modulus of the rock sample is 25.0 GPa. The contact parameters of platen-rock and rock-rock also follow the Brazilian tests. Three loading rates, v_y=2 mm/s, 5 mm/s and 10 mm/s, are respectively applied to the upper and lower platens. The mechanical responses of rock samples under different loading rates are given in Figure 15. It is obvious that all rock samples show brittle failure, and the lowest uniaxial compressive strength can be observed from the test with the smallest loading rate.

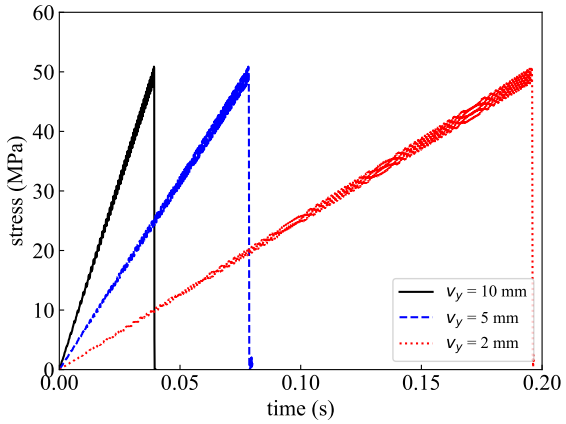

Figure 15: Stress-time curves under different loading rates

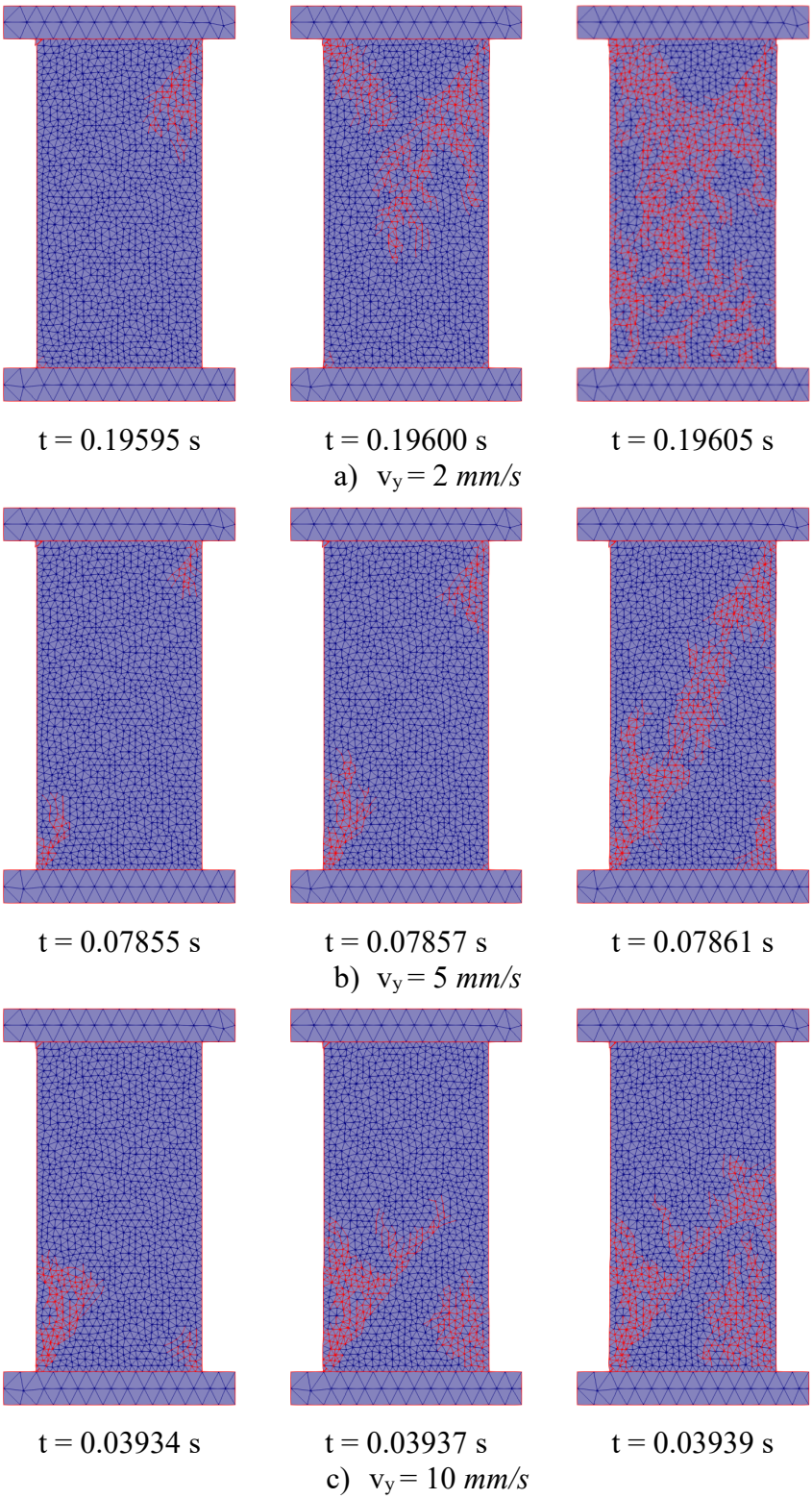

Figure 16: Fracture distributions under different loading rates

Figure 16 shows the snapshots of fracturing, colored by red, of rock samples with the initial mesh size being 4 *mm* under different compressive loading rates. We can see that the initiation of fractures and subsequent propagation are of great differences in the rock samples under different loading rates. However, it is evident that these fractures are all shear failure induced, because they propagate mainly along the shear zone formed

in the compression process.

4. Discussions

In this work, it has been demonstrated that the simulation performed using the continuum-based FDEM in conjunction with the inter-element fracture algorithm converges with the decrease of element sizes. For an accurate simulation of fracturing process a very fine mesh is required, especially in the area around the fracture tip. However, it is unknown where the fracture initiates within the continuum in most cases. In such a situation, the whole simulation domain needs to be discretized using fine meshes, which may be computationally expensive. To improve the computational efficiency of the continuum-based FDEM, an intra-element fracture algorithm was proposed by Prof. Owen's group at Swansea University, UK. We adapt the intra-element fracture algorithm in this work, and examine its efficiency in the Brazilian tests, uniaxial tension and compression tests of rock. It is found that the intra-element fracture algorithm can improve the numerical accuracy of the fracturing process in the simulations with a relatively large mesh size compared to the inter-element fracture algorithm in the framework of continuum-based FDEM. In the inter-element fracture algorithm, the fracture can only propagate along the edges of elements. For a simulation with a relatively large element size, the failure plane could pass through the element. If the fracture is only allowed to propagate along element edges, there will be numerical errors caused unless a very fine mesh is adopted. In contrast, the intra-element fracture algorithm can secure the accurate simulation of fracturing process. This has been evaluated in the above benchmark tests. In the Brazilian tests, the indirect tensile strength obtained from simulations with large element sizes and the intra-element fracture algorithm is only improved to a certain degree compared to the one obtained by the inter-element fracture algorithm.

One potential concern is that if very small-sized elements are created by the intra-element fracture algorithm, it may result in an extremely small time step and subsequently leads to very expensive computational costs. To quantify this concern, the computational efficiency of the continuum-based FDEM using different fracture algorithms and different element sizes is examined. The total CPU costs of all the numerical simulations of the Brazilian tests are compared in Figure 17, where the simulations are carried out in a laptop with Intel Core i5-6200U CPU @ 2.30GHz-2.40GHz and 8 GB memory (RAM).

It is shown that with the decrease of element sizes, the computational cost increases dramatically in both the inter-element and intra-element fracture algorithm groups. For the simulations with element sizes of 1 mm and 2 mm, there is no distinct difference in computational costs between the two algorithms, simply because fractures only propagate along element edges when element sizes are sufficiently small. While for the simulations with element sizes ranging from 4 mm to 5 mm, the computational cost of the simulations using the intra-element fracture algorithm is more expensive than the simulations using the inter-element fracture algorithm. However, compared to the accurate simulations using smaller element sizes, the increased time cost caused by the intra-element fracture in the simulations with relative larger elements can be ignored, which indicates that the intra-element fracture algorithm is more efficient. It is worth mentioning that to further improve the computational efficiency of the intra-element fracture algorithm, both global and local remeshing techniques can be employed to avoid elements with smaller characteristic sizes. Related work can be found in (Yu, 1999; Klerck et al., 2004).

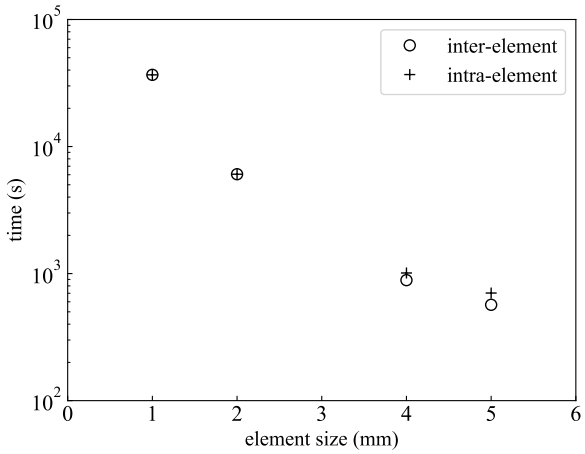

Figure 17: Computational costs used in the Brazilian tests

5. Conclusions

This work presents an improved continuum-based FDEM by the incorporation of shear failure induced fractures. Both the inter-element and intra-element fracture algorithms are developed. In particular, we also propose an improved intra-element fracture algorithm for fractures induced by both tensile and shear failure criteria. Then, benchmark tests, the Brazilian test, the uniaxial tension and compression tests of rock, are carried out to demonstrate our improved continuum-based FDEM. Conclusions can be drawn as follows:

1) Compared to the DEM-based FDEM, the continuum-based FDEM is more solid in theory, but its implementation is difficult and very challenging for three-dimensional simulations.

2) The simulated mechanical behavior of rock by the continuum-based FDEM with the inter-element fracture algorithm converges when element size decreases.

3) Benchmark tests prove that the intra-element fracture algorithm is more efficient in both computational cost and numerical accuracy compared to the inter-element fracture algorithm in the framework of continuum-based FDEM.

Obviously, more work, including detailed investigations of the model and related algorithms, is needed to further evaluate and improve the current two-dimensional FDEM. As we mentioned in the previous sections, some of the algorithms, such as the one to remove abnormal and slender elements, are only for 2-d problems, and their extension to 3-d models is not straightforward. Besides, to further improve the computational efficiency of the intra-element fracture algorithm, adaptive remeshing techniques are required for the simulations of engineering problems, which will be our future work.

Acknowledgment

The authors are grateful to the financial support from the National Natural Science Foundation of China under Grant No. 41931289 and the National Key Research and Development Program of China under Grant No. 2020YFC1808104.

References

Bažant, Z.P., Oh, B.H., 1983. Crack band theory for fracture of concrete. Matériaux et construction 16, 155–177.

De Borst, R., 1986. Computational aspects of smeared crack analysis computational modelling of rc structures (hinton e. and owen drj (eds)), chapter 2.

Feng, Y., 2021. An energy-conserving contact theory for discrete element modelling of arbitrarily shaped particles: Basic framework and general contact model. Computer Methods in Applied Mechanics and Engineering 373, 113454.

Feng, Y., Tan, Y., 2020. On minkowski difference based contact detection in discrete/discontinuous modelling of convex polygons/polyhedra: Algorithms and implementation. Engineering computations 37, 54–72.

Fu, P., Johnson, S.M., Carrigan, C.R., 2013. An explicitly coupled hydro-geomechanical model for simulating hydraulic fracturing in arbitrary discrete fracture networks. International Journal for Numerical and Analytical Methods in Geomechanics 37, 2278–2300.

Guo, L., Xiang, J., Latham, J.P., Izzuddin, B., 2016. A numerical investigation of mesh sensitivity for a new three-dimensional fracture model within the combined finite-discrete element method. Engineering Fracture Mechanics 151, 70–91.

Hamdi, P., Stead, D., Elmo, D., 2014. Damage characterization during laboratory strength testing: a 3d-finite-discrete element approach. Computers and Geotechnics 60, 33–46.

Han, K., Peric, D., Owen, D., Yu, J., 2000. A combined finite/discrete element simulation of shot peening processes–part ii: 3d interaction laws. Engineering Computations 17, 680–702.

Joulin, C., Xiang, J., Latham, J.P., 2020. A novel thermo-mechanical coupling approach for thermal fracturing of rocks in the three-dimensional fdem. Computational Particle Mechanics , 1–12.

Ju, Y., Wang, Y., Chen, J., Gao, F., Wang, J., 2018. Adaptive finite element-discrete element method for numerical analysis of the multistage hydrofracturing of horizontal wells in tight reservoirs considering pre-existing fractures, hydromechanical coupling, and leak-off effects. Journal of Natural Gas Science and Engineering 54, 266–282.

Klerck, P., Sellers, E., Owen, D., 2004. Discrete fracture in quasi-brittle materials under compressive and tensile stress states. Computer methods in applied mechanics and engineering 193, 3035–3056.

Knight, E.E., Rougier, E., Lei, Z., Euser, B., Chau, V., Boyce, S.H., Gao, K., Okubo, K., Froment, M., 2020. Hoss: an implementation of the combined finite-discrete element method. Computational Particle Mechanics , 1–23.

Lei, Q., Latham, J.P., Xiang, J., 2016. Implementation of an empirical joint constitutive model into finite-discrete element analysis of the geomechanical behaviour of fractured rocks. Rock Mechanics and Rock Engineering 49, 4799–4816.

Li, D., Wong, L.N.Y., 2013. The brazilian disc test for rock mechanics applications: review and new insights. Rock mechanics and rock engineering 46, 269–287.

Morris, J.P., Rubin, M., Block, G., Bonner, M., 2006. Simulations of fracture and fragmentation of geologic materials using combined fem/dem analysis. International Journal of Impact Engineering 33, 463–473.

Munjiza, A., 1992. Discrete elements in transient dynamics of fractured media. Ph.D. thesis. Swansea University, UK.

Munjiza, A., Andrews, K., White, J., 1999. Combined single and smeared crack model in combined finite-discrete element analysis. International journal for numerical methods in engineering 44, 41–57.

Munjiza, A., John, N., 2002. Mesh size sensitivity of the combined fem/dem fracture and fragmentation algorithms. Engineering Fracture Mechanics 69, 281–295.

Munjiza, A., Owen, D., Bicanic, N., 1995. A combined finite-discrete element method in transient dynamics of fracturing solids. Engineering computations 12, 145–174.

Munjiza, A., Rougier, E., Lei, Z., Knight, E.E., 2020. Fsis: a novel fluid–solid interaction solver for fracturing and fragmenting solids. Computational Particle Mechanics , 1–17.

Munjiza, A.A., 2004. The combined finite-discrete element method. John Wiley & Sons.

Owen, D., Feng, Y., 2001. Parallelised finite/discrete element simulation of multi-fracturing solids and discrete systems. Engineering computations 18, 557–576.

Pande, G., Pietruszczak, S., Wang, M., 2020. Role of gradation curve in description of mechanical behavior of unsaturated soils. International Journal of Geomechanics 20, 04019159.

Pietruszczak, S., 2010. Fundamentals of plasticity in geomechanics. Crc Press Boca Raton, FL.

Profit, M., Dutko, M., Yu, J., Cole, S., Angus, D., Baird, A., 2016. Complementary hydro-mechanical coupled finite/discrete element and microseismic modelling to predict hydraulic fracture propagation in tight shale reservoirs. Computational Particle Mechanics 3, 229–248.

Rockfield, 2004. ELFEN 2D/3D numerical modelling package. Rockfield Software Ltd. Swansea, UK.

Rougier, E., Munjiza, A., Lei, Z., Chau, V.T., Knight, E.E., Hunter, A., Srinivasan, G., 2020. The combined plastic and discrete fracture deformation framework for finite-discrete element methods. International Journal for Numerical Methods in Engineering 121, 1020–1035.

Settgast, R.R., Fu, P., Walsh, S.D., White, J.A., Annavarapu, C., Ryerson, F.J., 2017. A fully coupled method for massively parallel simulation of hydraulically driven fractures in 3-dimensions. International Journal for Numerical and Analytical Methods in Geomechanics 41, 627–653.

Wang, Y., Ju, Y., Chen, J., Song, J., 2019. Adaptive finite element–discrete element analysis for the multistage supercritical co2 fracturing and microseismic modelling of horizontal wells in tight reservoirs considering pre-existing fractures and thermal-hydro-mechanical coupling. Journal of Natural Gas Science and Engineering 61, 251–269.

Yan, C., Jiao, Y.Y., 2019. Fdem-th3d: A three-dimensional coupled hydrothermal model for fractured rock. International Journal for Numerical and Analytical Methods in Geomechanics 43, 415–440.

Yu, J., 1999. A contact interaction framework for numerical simulation of multi-body problems and aspects of damage and fracture for brittle materials. Ph.D. thesis. Swansea University, UK.